Available online at www.sciencedirect.com

ScienceDirect

Comput. Methods Appl. Mech. Engrg. 276 (2014) 396–409

Computer methods in applied mechanics and engineering

www.elsevier.com/locate/cma

A feature extracting and meshing approach for sheet-like structures in rocks

Yan Liu, H.L. Xing *

Centre of Geosciences Computing, School of Earth Sciences, The University of Queensland, St. Lucia, QLD 4072, Australia

Received 14 October 2013; received in revised form 21 January 2014; accepted 28 March 2014
Available online 13 April 2014

Abstract

Meshing rock samples with sheet-like structures based their CT scanned volumetric images, is a crucial component for both visualization and numerical simulation. In rocks, fractures and veins commonly exist in the form of sheet-like objects (e.g. thin layers and distinct flat shapes), which are much smaller than the rock mass dimensions. The representations of such objects require high-resolution 3D images with a huge dataset, which are difficult and even impossible to visualize or analyze by numerical methods. Therefore, we develop a microscopic image based meshing approach to extract major sheet-like structures and then preserve their major geometric features at the macroscale. This is achieved by the following four major steps: (1) extracting major objects through extending, separation and recovering operations based on the CT scanned data/microscopic images; (2) simplifying and constructing a simplified centroidal Voronoi diagram on the extracted structures; (3) generating triangular meshes to represent the structure; (4) generating volume tetrahedron meshes constrained with the above surface mesh as the internal surfaces. Moreover, a shape similarity approach is proposed to measure and evaluate how similar the generated mesh models to the original rock samples. It is applied as criteria for further mesh generation to better describe the rock features with fewer elements. Finally, a practical CT scanned rock is taken as an application example to demonstrate the usefulness and capability of the proposed approach.

Keywords: 3D image; Feature extraction; Unstructured mesh generation; Fractures; Rock veins; Sheet-like structure

1. Introduction

An increasingly used source of information describing rock samples is obtained in the form of 3D images scanned from realistic entities by using the advanced imaging technology such as the computed tomography (CT) and the magnetic resonance imaging (MRI). Sheet-like structures (e.g. fractures and veins) widely distributed in rocks are important sources of material heterogeneity and thus should be particularly addressed

* Corresponding author. Tel.: +61 7 33464093.
E-mail address: h.xing@uq.edu.au (H.L. Xing).

http://dx.doi.org/10.1016/j.cma.2014.03.020
0045-7825/

for better evaluating the geomechanical and flow behaviors. Due to easy generation of regular mesh, most numerical simulations for volumetric rock images are based on finite difference method [1] and/or lattice Boltzmann method [2]. While finite element method has more advantages over the finite different method for the complicated structure analysis especially for those with faults/fractures and sheet-like structures [3,4]. However, the related unstructured mesh generation remains a quite challenging topic.

Image-based sheet-like structure meshing relies on high quality digital image. Rocks are usually made up of many constituents, ambiguities may happen if there is no prior knowledge about the constructive minerals. Besides, partial volume effect is another reason for generating poor quality digital images. Digital imaging such geomaterials is difficult in itself but gets achievable [5–7]. Segmentation algorithms [8], together with the CT imaging techniques, are critical for labeling different rock objects and describing fracture structures. Such algorithms may be sensitive to the local image noise and could not produce reasonable results for the sheet-like structures due to the thin features if without high enough resolution [9]. Therefore, high-resolution volumetric images are utilized to capture such geometric features, but such high resolution images lead to a huge dataset, which may be out of current computer capability to analyze and even visualize [10,11]. Thus there is an emerging need for generating analysis-suitable meshes for the segmented rock images involving sheet-like structures, which is also the research focus of this paper.

The mesh generation for 3D images has been studied in many communities [12,13] (e.g. visualization, medical imaging and FEM-based simulation) and is an active subject of a number of on-going studies [5,14–18]. For meshing 3D images, the simplest way is to directly convert voxels into brick elements [14]. However, the drawbacks of this method are evident, besides of the huge dataset generated, the jagged boundaries lead to poor results and even errors in simulations [19]. Marching cubes method [20] and its extensions [15,21,22] are developed to capture interface surfaces and further smooth them for multi-material volumetric dataset. These algorithms suffer from topological defects, ambiguous structures, and an exponential growth in the element numbers with respect to its grid resolution. Alternate image meshing approaches [16,17] based on a Delaunay refinement method are recently studied to identify material interfaces and preserve the geometric features. As the sheet-like objects cause opposite boundaries to be close to each other, there is no guarantee for the topological correctness of the mesh generated by Delaunay triangulation. Therefore, such approaches are not acceptable for the problems addressed here. Zhang et al. [5,23] innovatively proposed an octree-based approach to generate meshes from images. They also designed a surface smoothing strategy [24] to improve the boundary element quality. The advantage of their approach is the ability of creating quality hexahedral elements from images. However, automatic hexahedral mesh generation for complex structures is still difficult and unachievable. In general, the mesh generation for sheet-like structures in rocks is still challenging and current image meshing methodologies in computational medicine and biology are not necessarily suitable for meshing fractures and veins.

Based on the surface meshes generated by marching cubes methods [15,20], mesh coarsening approaches can further reduce the element number. The existing coarsening algorithms could be roughly classified into three groups: decimation, scattering and remeshing. The decimation approach [25,26] reduces the number of elements through a series of elementary simplifications such as collapsing edge and merging face. These operations are efficient but they could produce a number of thin or flat elements leading to poor mesh quality. The Vertex scattering technique [27,28] is to firstly scatter vertices on the surface and then smooth these vertices until a given precision is achieved. Comparing with the decimation method, it could generate high quality mesh but is quite time-consuming due to the large number of background element required. The remeshing approach [29–32] could coarsen meshes with a desired element gradation through a parameterized space, which requires the background surface mesh could be well partitioned. Although these coarsening approaches could decrease element numbers of the surface mesh, they are not suitable for the problems addressed here.

A better representation for a sheet-like structure is surface mesh to represent such a thin object. Therefore, it is necessary to develop a rock image based meshing approach to extract sheet-like structures (major fractures and veins) in rocks and describe them with approximated surface meshes, which ensure capture their major geometric features by using a limited number of high quality elements.

2. Implementation for feature extracting and image meshing

The advanced imaging technologies such as CT and MRI all produce 3D images for describing rocks with complicated structures in more details. The 3D micro-CT scanned rock image used here is formed from a stack of 2D images in Fig. 1. The unit of 3D image is voxel analogous to pixel in 2D, which has a position as well as a scalar value representing its material/colour. There scalar values subdivide the volume into regions representing different components of the scanned rock such as fractures, veins and matrix. The fractures and veins are known as sheet-like objects, one of their dimensions is much smaller than the other two.

2.1. Simplified centroidal Voronoi diagram (SCVD) construction for sheet-like structures

Given an open set $\Omega \subseteq \mathbb{R}^N$, and n different generators $\{z_i\}_{i=1}^n$. Let $dis(\cdot)$ denote the distance function on $\mathbb{R}^N$, the Voronoi diagram (whose dual is well-known as Delaunay triangulation) is defined as $\{V_i\}_{i=1}^n$:

$$V_i = \{x \in \Omega |\ dis(x, z_i) < dis(x, z_j) \text{ for } j = 1, \ldots, n,\ j \neq i\} \tag{1}$$

Centroidal Voronoi diagram is firstly proposed by Du et al. [33] where the generator z_i is also the mass centroid of its Voronoi cell:

$$z_i = \frac{\int_{V_i} x \cdot \rho(x) dx}{\int_{V_i} \rho(x) dx} \tag{2}$$

where $\rho(x)$ is a density function of V_i.

In this section, a simplified centroidal Voronoi diagram is proposed based on volumetric dataset. In 3D rock images, sheet-like objects are represented by a set of voxels sharing the same volume and density, so in the proposed SCVD construction $\rho(x) = 1$ for Formula 2. As the objects have a small thickness and are somehow equivalent to a plain, we construct Voronoi diagram by propagating Voronoi cells from their generators in the manner of Breadth First Search (BFS). $dis(\cdot)$ indicates surface distance on sheet-like objects and Formula 1 is automatically satisfied in the process of BFS. Pseudo-code in Algorithm 1 describes the simplified Voronoi diagram construction where 6-voxel connectivity is employed. Take a patch in Fig. 2 for example, Fig. 2(a)–(c) are three stages from the generators to the final Voronoi cells.

Algorithm 1: simplified Voronoi diagram construction
Treat voxels linked with z_i as the initial Voronoi cell V_i
WHILE there is a voxel not belonging to $\{V_i\}_{i=1}^n$
  FOR EACH V_i *in* $\{V_i\}_{i=1}^n$
    Progress V_i by one voxel in the manner of BFS
  END
END

SCVD is an approximate implementation of centroidal Voronoi diagram, which bases on the theory proposed by Du et al. [33]. Firstly, n Voronoi generators $\{z_i\}_{i=1}^n$ are randomly selected from the voxels on sheet-like objects in rock images. Then locations of these generators are iteratively optimized by Formula 2 until the energy error [33] is achieved. The generator number n is calculated by the following formula.

$$n = \frac{C_{vol}}{V_{vol}}, \quad V_{vol} = t \cdot (1 + 2 \cdot r \cdot (r - 1)) \tag{3}$$

where C_{vol} is the total volume of the structure, t is the average thickness and r is the customized radius of a Voronoi cell. As C_{vol} and t are known, r is the only variable to define the generators as well as the SCVD.

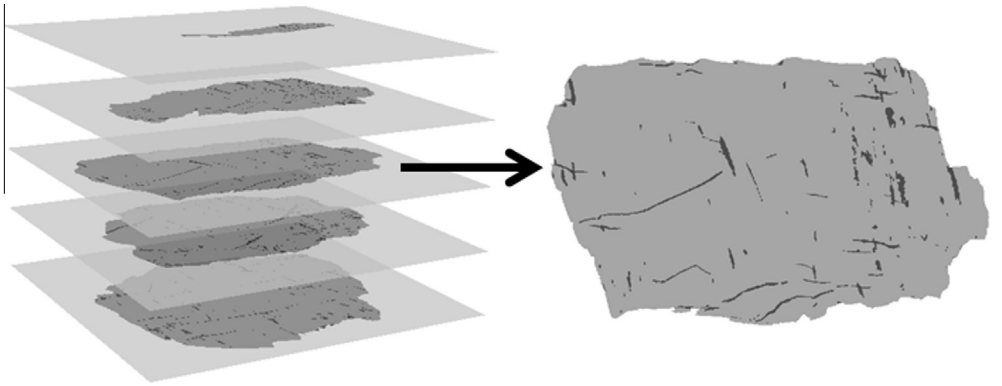

Fig. 1. The micro-CT scanned digital image of a rock block with the size of $1012 \times 1024 \times 931$. The matrix is in grey and sheet-like structures are in back.

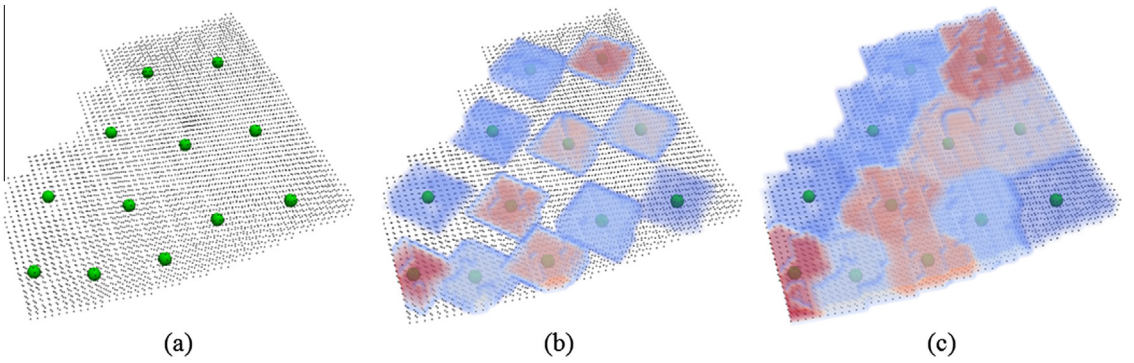

Fig. 2. Simplified Voronoi diagram construction: (a) a patch and its generators; (b) the growing Voronoi cells; (c) the finial Voronoi diagram.

2.2. Feature extraction

In practice, sheet-like objects have different sizes and shapes thus they affect the rock mechanical behavior in different ways. Feature extraction is necessary for the reduction of the structure complexity, which keeps major objects and removes small entities. The small entity removal is governed by a customized volume criterion M, which identifies disconnected objects smaller than M and removes them. Such a criterion will cause two problems in feature extraction: (1) major objects represented by a set of small entities will not be recognized and (2) small entities intersecting with major objects will not be removed. In this paper, an object represented by a number of small disconnected objects is named as potential object and a structure consisting of intersecting objects is called crossing structure. The workflow for the feature extraction is demonstrated in Fig. 3, where potential object detection and geometric feature recovery are achieved by extending operation, crossing structure separation is implemented by separation operation and dilation/erosion algorithms are involved in the above operations. The following of this section will focus on introducing separation and extending operations. As dilation/erosion algorithms [34] are general in image processing, they are not further discussed in this paper.

2.2.1. Separation operation

Before separation, dilation/erosion algorithm is involved to refine the sheet-like objects by a thickness t. Then we specify a Voronoi cell radius r and use Formula 3 to calculate Voronoi generator number. In practice, the choice of t and r depends on the sheet-like object morphology and the rock image resolution. In the next

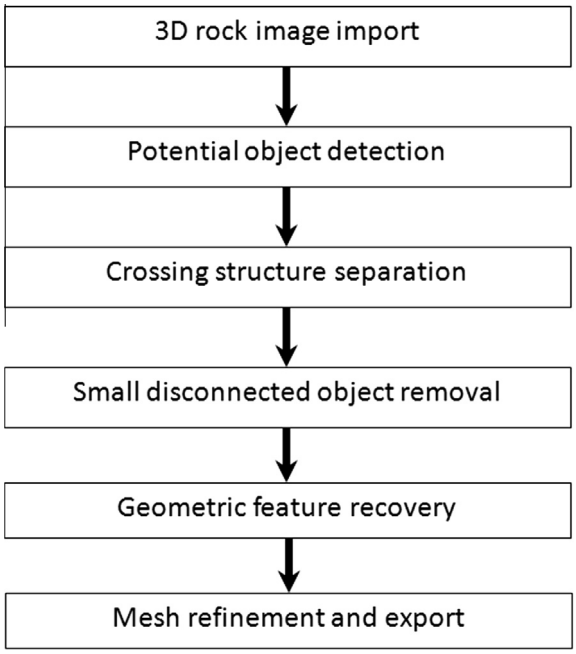

Fig. 3. Workflow for feature extraction.

step, we construct a SCVD on the crossing structures and generate corresponding triangles. The separation operation is achieved based on these triangles.

Algorithm 2: separation operation
D_{ang} is a customized dihedral angle threshold
A generator z is flat only if no dihedral angle between its linked triangles smaller than D_{ang}
FOR EACH z in $\{z_i\}_{i=1}^{n}$
IF z is marked ***CONTINUE***
IF z is not flat ***CONTINUE***
Mark z and put it into a set CZ
Increase CZ by its adjacent generators which are not marked but flat and mark the generators once they are pushed into CZ
Export CZ as a single piece
END

Specifically, we show the details of the separation operation on a pair of crossing patches in Fig. 4. Firstly, crossing patches are extracted from a 3D rock image as shown in Fig. 4(a). Then a SCVD is constructed in Fig. 4(b) by Algorithm 1 with $r = 5$. The number of generators in this diagram is 147 and corresponding triangles in Fig. 4(c) are generated. In the last step, we choose $D_{ang} = 150°$ and make the current structure apart by Algorithm 2. In fact, the separation operation removes voxels on the intersection. As shown in Fig. 4(d), the operation creates a hole on one patch which is labeled as A and breaks the other patch into two disconnected objects B and C.

2.2.2. Extending operation

For a patch, its tangent and normal directions are required for the extending operation in the processes of potential major object detection and geometric feature recovery. Nevertheless, such sheet-like objects in 3D images consist of a set of voxels that have no tangent or normal information. We apply triangles generated from the SCVD to extend the patches roughly along their tangent direction.

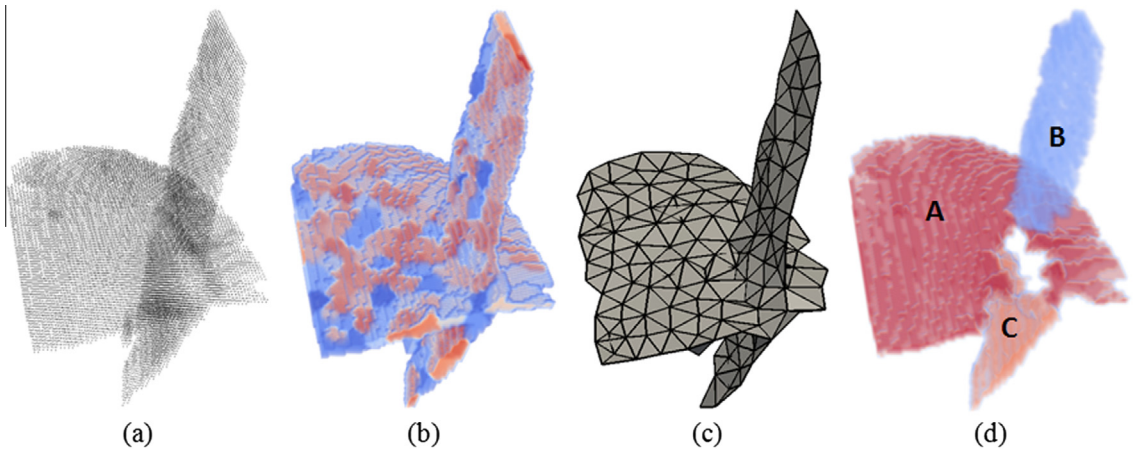

Fig. 4. Separation operation: (a) two patches intersecting with each other; (b) the SCVD; (c) the generated triangles; (d) three disconnected objects.

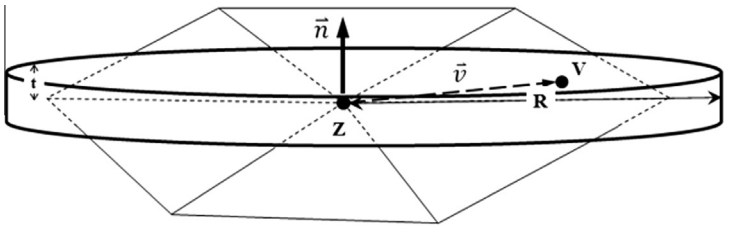

Fig. 5. Voxel predication for extending operation: V is a voxel to be predicated; Z is a generator and $\vec{n}$ is its normal; $\vec{v}$ is the vector from Z to V; the thickness is $2t$; R is a customized radius.

To extend a patch, the SCVD and its corresponding triangular mesh are previously constructed. In Fig. 5, Z is a generator and $\vec{n}$ is the normalized average normal of triangles linked Z. V is a voxel near Z and $\vec{v}$ is the vector from Z to V. The criterion of whether V could be extended is

$$\begin{cases} |\vec{v}\cdot\vec{n}| < t \\ \sqrt[2]{|\vec{v}|^2 - |\vec{v}\cdot\vec{n}|^2} < R \end{cases} \tag{4}$$

where $2t$ is the thickness of the patch and R is the customized radius for the extending operation. Z, t and R define a flat cylinder as shown in Fig. 5 and voxels acceptable for extension are within this cylinder. For the extending operation in geometric feature recovery, there is an additional criterion which is the potential voxel must belong to corresponding objects of the original digital image.

Applications of extending operation for potential object detection and geometric feature recovery are demonstrated in Figs. 6 and 7 respectively. Fig. 6(a) is a set of disconnected objects that are separated with each other. We use the parameters $t = 1.5$ and $R = 7$ to perform the extending operation in this application. From Fig. 6(a) to (c), the objects are roughly extended along their tangent directions and finally merged into one. Fig. 7(a) is the separated object A in Fig. 4(d) where the gap highlighted is produced by the separation operation. The gap is shrunk in Fig. 7(b) by the proposed extending operation using parameters $t = 1.5$ and $R = 7$. Fig. 7(c) is the result of this operation where the gap disappears and the geometric shape is recovered.

2.3. Mesh generation and shape similarity measurement

2.3.1. Surface and volume mesh generation

The surface mesh generation for the sheet-like structures is based on the SCVD. The generating route is similar to the Delaunay triangulation but ambiguities caused by the fuzzy cell boundaries in SCVD need to

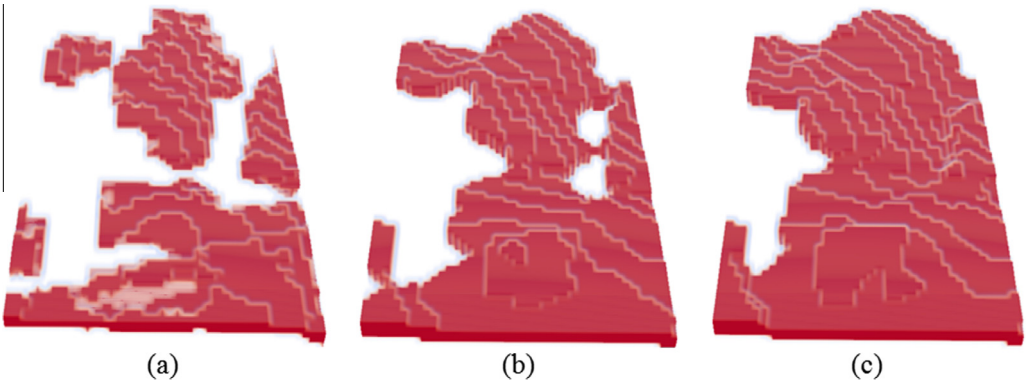

Fig. 6. Potential object detecting: (a) is several disconnected objects in the rock image; from (a) to (c) these objects are merged into a whole piece through the extending operation.

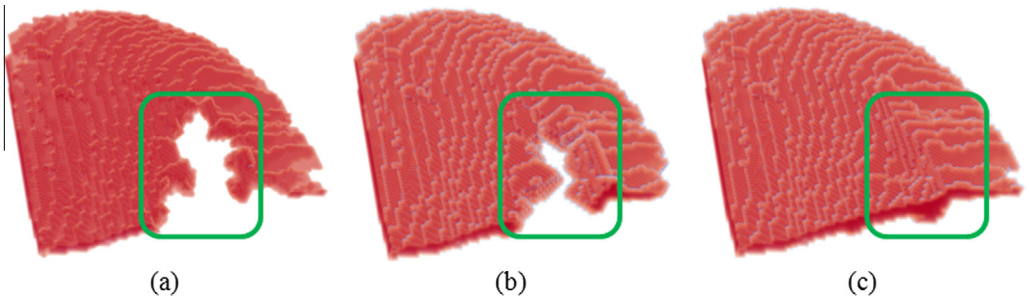

Fig. 7. Geometric feature recovery: (a) is the disconnected object in Fig. 4(d); from (a) to (c) the geometric feature is recovered by the extending operation.

be further refined. In Fig. 8, *A*, *B*, *C* and *D* represent IDs of Voronoi cells and the dots represent voxels within a cubic. For a regular case, in Fig. 8(a), there are only three IDs in the cubic and a triangle is constructed by connecting the corresponding generators. For an ambiguous case, in Fig. 8(b), more than three IDs exist in the cubic and the constructed triangles will cause a topological defect.

An amending strategy is proposed here to remove such ambiguity in triangular element construction. As shown in Fig. 9(a), the SCVD has four generators *A*, *B*, *C* and *D* and the ambiguity is highlighted in a black circle. The amending strategy is processed during the SCVD construction. Specifically, two generators are

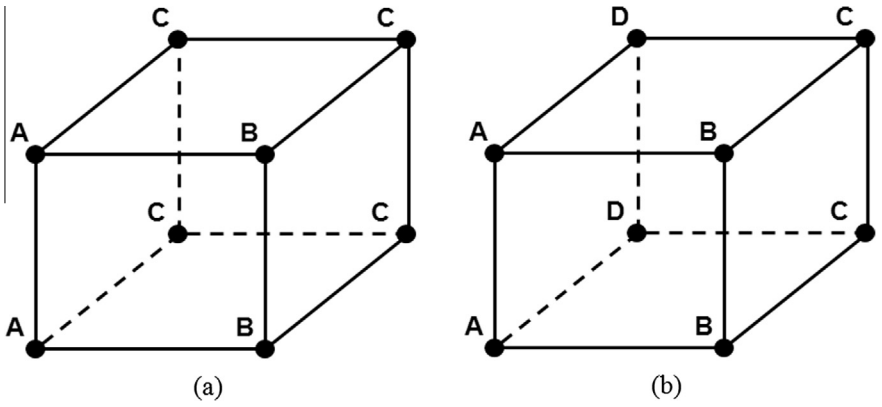

Fig. 8. Triangular element construction: (a) a regular case and (b) an ambiguous case.

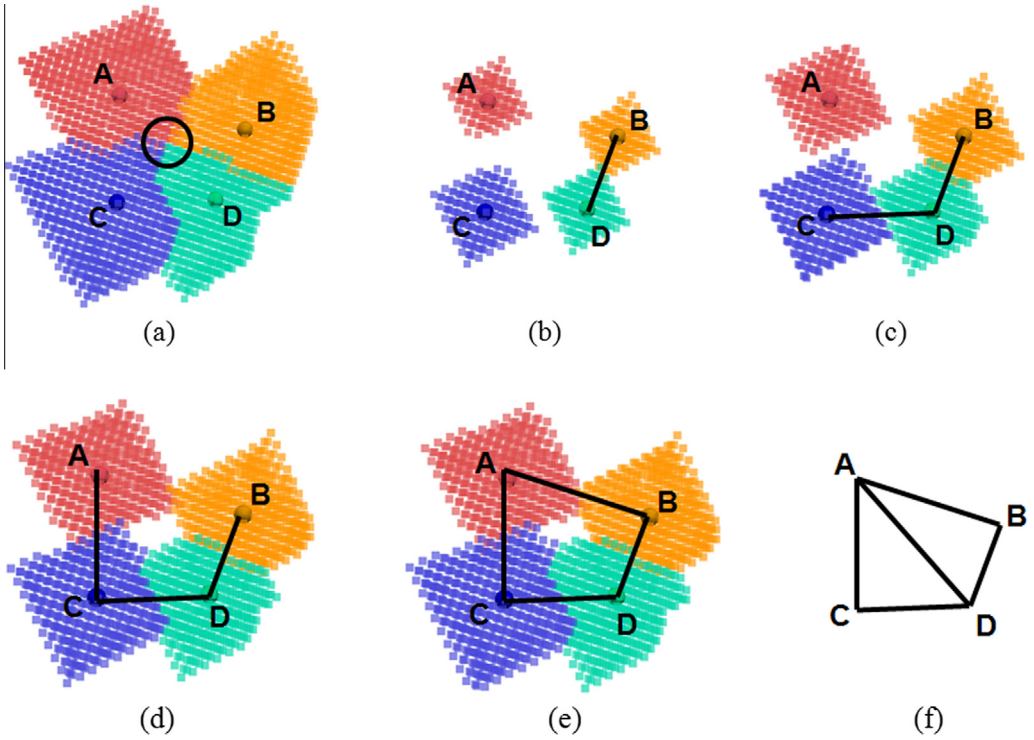

Fig. 9. Amending strategy for triangular element construction: (a) the SCVD with ambiguity; (b)–(f) the proposed amending process.

connected whenever their corresponding Voronoi cells meet each other in the propagation. In Fig. 9(b)–(e), *B–D*, *C–D*, *A–C* and *A–B* are connected serially and a polygon *ABCD* is constructed simultaneously. Based on the polygon, triangles *ACD* and *ABD* in Fig. 9(f) are created.

We serve the generated triangular meshes serve constraints then apply a constrained Delaunay tetrahedralization to generate the corresponding volume mesh. The whole mesh generation procedure is demonstrated in Fig. 10(a)–(c) with the following steps: (1) constructing SCVD; (2) constructing triangular mesh for the object; (3) generating volume mesh through Delaunay tetrahedralization with vein surface constraints.

2.3.2. Shape similarity measurement

Shape similarity measurement is crucial for evaluating how the generated mesh model is close to the input 3D image. For a surface mesh, each element has a thickness value, which is gained from the input image. Specifically, each voxel belonging to sheet-like structure has a thickness value, obtained by the smallest thickness in its three directions. The thickness of a triangular element is the average thickness of voxels intersecting with it. Letting the triangle be the mid plane and its thickness be the height, a prism is constructed for the element. We convert each element of the surface mesh to a volumetric representation by labeling voxels within its prism. Then a volumetric description of the surface mesh is generated. Compared with the input image, voxels of the mesh volumetric representation could be grouped into two sets: C^{in}_{mesh} coincident with the input image and C^{out}_{mesh} different from the input image. Taking into account both C^{in}_{mesh} and C^{out}_{mesh}, a similarity measurement is defined as:

$$\text{Similarity} = \frac{|C^{in}_{mesh}| - |C^{out}_{mesh}|}{|C_{image}|} \tag{5}$$

where C_{image} is the set of sheet-like objects in the input image and operator $|\cdot|$ calculates the number of voxels. The range of the similarity is $[1.0, -\infty]$ and a larger value denotes better matching with the original data.

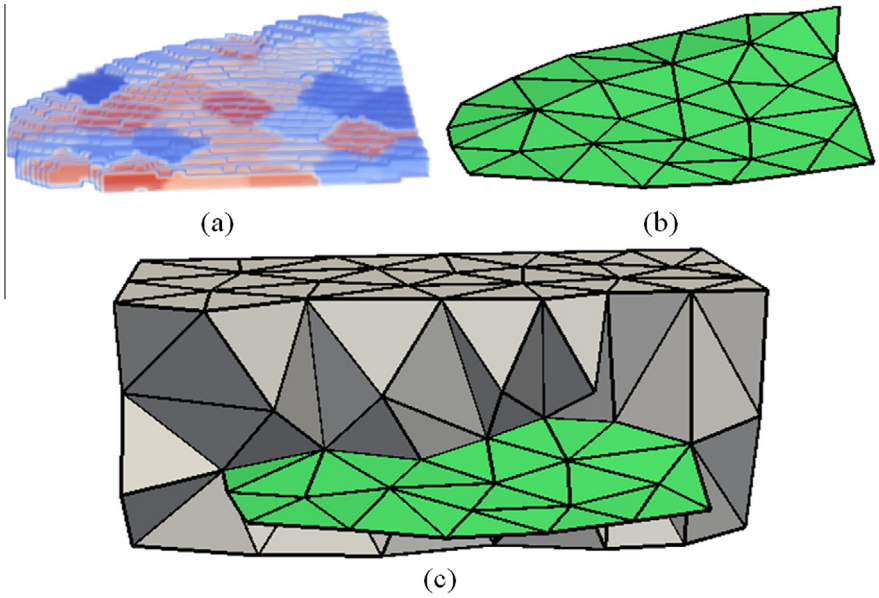

Fig. 10. Mesh generation: (a) the SCVD; (b) the triangular mesh; (c) the volume mesh with surface constraints.

3. Numerical applications

The proposed sheet-like structure extraction and related mesh generation approaches are designed for 3D rock images with complex fractures and veins. Numerical applications based on scanned rock images in practice are presented as below to demonstrate these techniques in detail.

The first example (Fig. 11) is a part of sheet-like objects extracted from a 3D rock image. The major structure consists of patches with different sizes and a number of holes/gaps as shown in Fig. 11(a). Firstly, the extending

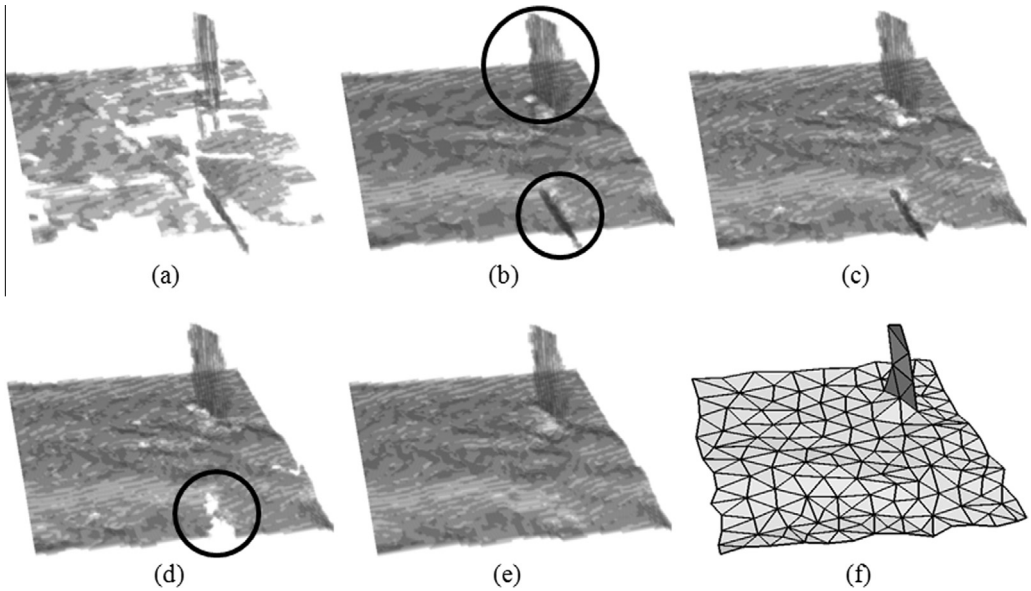

Fig. 11. Sheet-like object extraction and its surface mesh generation: (a) the input objects; (b) detected major entities; (c) structure separation; (d) minor objects removal; (e) geometric recovery; (f) the surface mesh.

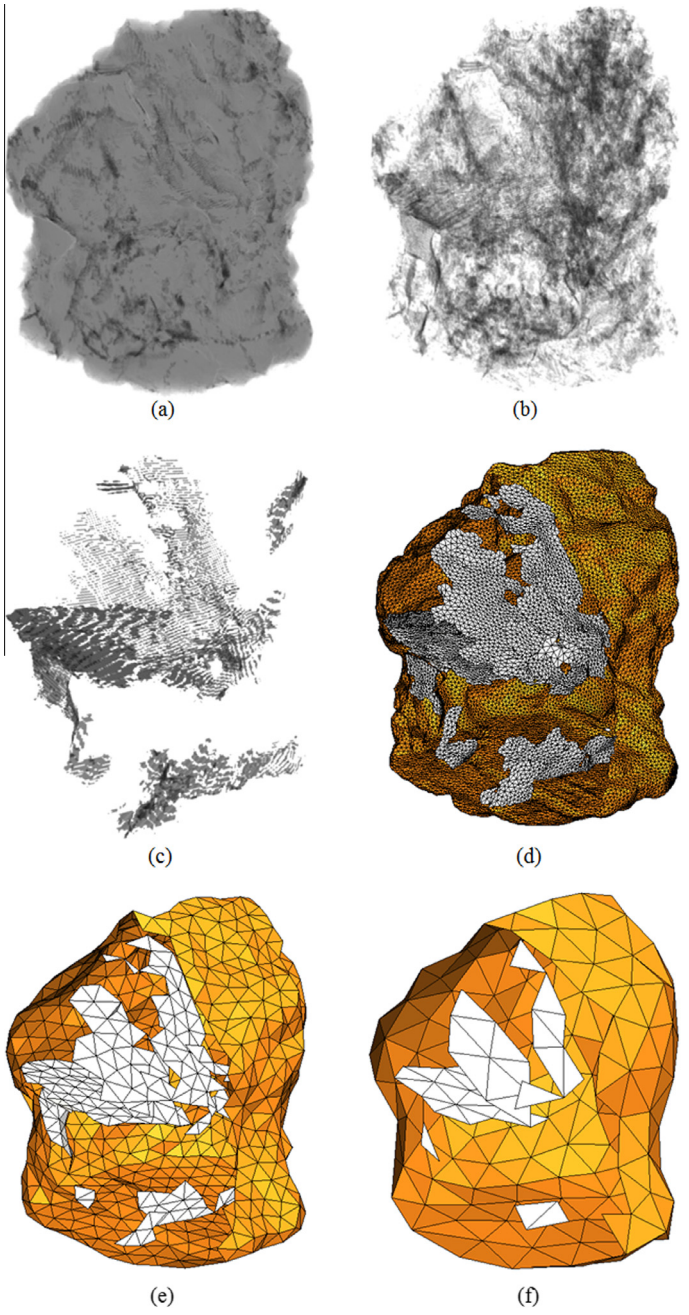

Fig. 12. A 3D rock image meshed with different element sizes: (a) the 3D rock image with the size of $1012 \times 1024 \times 931$; (b) the internal sheet-like structures; (c) the major objects; (d)–(f) are triangular meshes generated by different Voronoi cell radii where the major sheet-like objects are in white and the outside rock boundaries are in golden.

operation is applied to detecting potential major entities and the result is shown in Fig. 11(b). The detected objects including a big flat shape and two small patches (highlighted in black circles) intersect with each other. In the next step, the structure is separated into several pieces and the progression itself generates gaps (in Fig. 11(c)) at the intersection where objects meet. In Fig. 11(d), the smallest piece is removed, which induces a gap highlighted by a black circle on the big object. In the next stage, the gap is filled by the geometric recovery

process and the major structure of the objects is clearly identified in Fig. 11(e). Finally, a triangular surface mesh is generated in Fig. 11(f), which approximates the major structures in Fig. 11(a).

The second example is a rock image with the size of $1012 \times 1024 \times 931$ in 3D (Fig. 12(a)). The rock has complex internal structures as shown in Fig. 12(b). The major objects extracted in Fig. 12(c) are utilized to represent the model for the further analysis. Figs. 12(d)–(f) show the ability of the proposed method to control element size and quantity in meshing rock images (where sheet-like objects are in white and rock boundaries are in golden). Table 1 gives an overview of element size, number and similarity between the meshes and its 3D image model in Fig. 12(c). The features of the generated mesh is controlled by Voronoi cell radius r in Formula 3, where with the increasing of r, the element number is reduced, but the similarity is also decreased (Table 1).

A chart in Fig. 13 is obtained through meshing the rock structures in Fig. 12(c), which further reveal the relationship between Voronoi cell radius r and the corresponding mesh similarity. One important aspect must be mentioned is the thickness of the objects. On one hand, once r is close or less than the thickness the proposed algorithm assembles the structure into small pieces (due to D_{ang} in Algorithm 2) which will be later removed. On the other hand, if r is much larger than the thickness some details of the structure are lost. As the average thickness of the objects in Fig. 12(c) is 5, Voronoi cell radius $r = 7$ is the best choice with respect to the highest shape similarity 64.57%, which generates a surface mesh with 69,394 elements. Considering the image models in the form of grids, evenly sampling the grids to reduce image resolution could simplify the model and reduce its dataset scale, but the similarity will drop dramatically as shown in Table 2. Additionally, the resolution reduction approach is not as effective as the proposed image meshing algorithm in representing sheet-like structures for visualization. Compared with the mesh model with $r = 7$, grid models

Table 1
Summary for surface meshes in Fig. 12(d)–(f).

Fig. 12	(d)	(e)	(f)
Voronoi cell radius	11	51	107
Element size	14.88	66.49	135.75
Element number	40204	1777	368
Similarity	63.28%	29.46%	11.66%

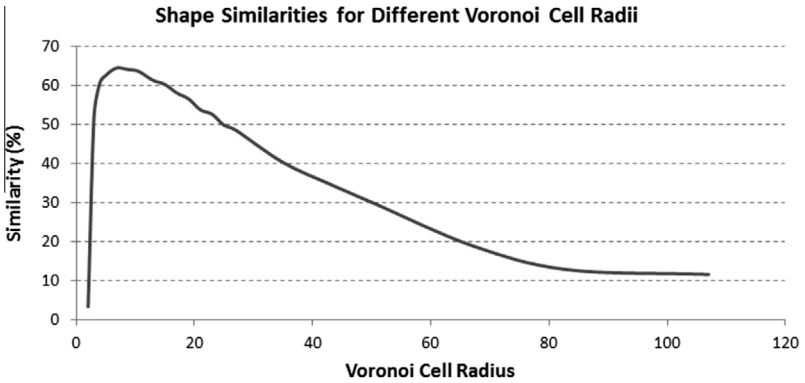

Fig. 13. Relationship between shape similarity and Voronoi cell radius: the highest similarity is 64.57% when the Voronoi cell radius is 7.

Table 2
Grid model for Fig. 12(c) with different sample rates.

Sample rate	1	2	3	4	$\geqslant 5$
Similarity	100.0%	65.5%	37.8%	15.4%	$\leqslant$0.0%
Grid quantity	9.6×10^8	1.2×10^8	3.6×10^7	1.5×10^7	7.7×10^6

whose sampling rates are larger than 2 have a lower similarity and a larger grid number. Although the similarity of grid model with sampling rate 2 is comparable with the mesh mode similarity, its grid quantity is 9.6×10^8 which is 1.4×10^4 times as much as that in the mesh model.

Besides visualization, another important application of the proposed method is numerical simulation, which needs a volume mesh model rather than a surface mesh to describe the rock and its sheet-like structures. Mesh with shape similarity above 60% could be considered as an acceptable approximation of the rock image. According to the chart in Fig. 13, we choose surface meshes generated by $r = 15$ where the similarity is 60.3% and the mesh for the major sheet-like structure is individually shown in Fig. 14(a). In fact, the proposed similarity calculation method is a strict measurement. Fig. 14(b) includes both the surface mesh Fig. 14(a) and the input 3D image Fig. 12(c), where the mesh almost completely approximates the structure from the aspect of visualization. Fig. 14(c) is the surface mesh with its thickness property. Elements with 0 thickness indicate holes or gaps for the input image model. Taking the surface mesh and corresponding rock boundaries as con-

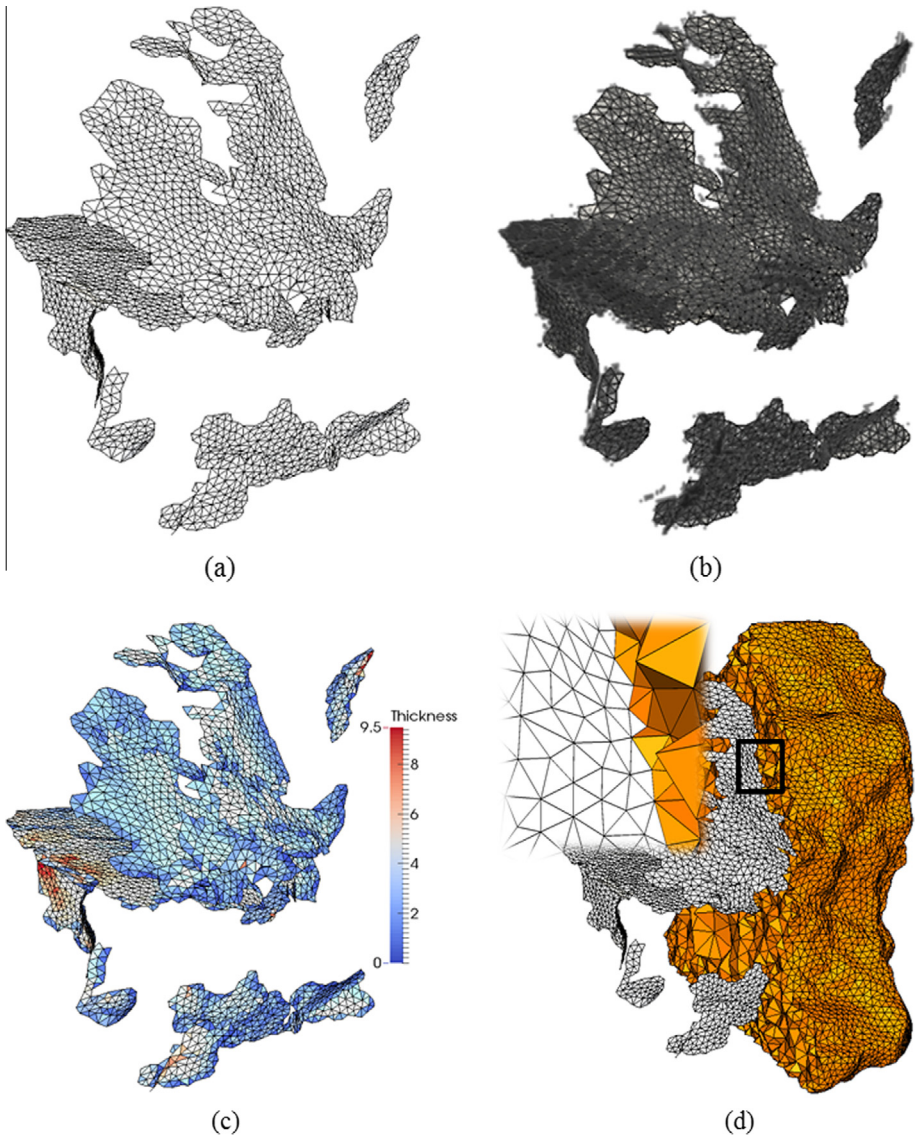

Fig. 14. Mesh generation for a rock image: (a) surface mesh of the main structure; (b) surface mesh with the input image; (c) surface mesh with thickness property and (d) the volume mesh with 28,631 nodes and 143,901 elements.

Table 3
Element quality for Fig. 14(d).

Quality measurement	Minimum quality	Average quality	Regular tetrahedron
Minimum dihedral angle	8.18°	49.06°	70.53°
Gamma quality	0.14	0.81	1.00
Edge aspect	0.20	0.66	1.00
Radius aspect	0.06	0.84	1.00

straints, a tetrahedral mesh Fig. 14(d) is constructed by the in-house developed mesh generator. The surface mesh is consistent with the volume mesh, shown in the close-up in Fig. 14(d). The volume mesh has 28,631 nodes as well as 143,901 elements. In general, compared with grid models, the generated volume mesh achieves a better similarity with fewer elements with respect to Table 2.

In Table 3, four methods [35,36] are adopted to measure the element quality of the generated volume mesh in Fig. 14(d). Statistics in Table 3 show that the average element qualities of the generated mesh are close to the regular tetrahedron. Consequently, the generated volume mesh model is considered as analysis-suitable for finite element simulation.

4. Conclusions

In this paper, a new mesh generation approach for 3D rock images with fractures and veins is proposed to generate both surface and volume meshes for rocks involving complicated sheet-like structures. Comparing with grid models, the proposed algorithm can generate meshes with less element number to approximate internal sheet-like structures within rock samples. For the rock sample, the ratio between the tetrahedral mesh element number and the grid number is 1:6704. A shape similarity measurement is also proposed and the optimal Voronoi cell radius used for generating surface mesh for the rock sample is 7 with the corresponding similarity 64.57%. In practice, surface meshes with shape similarity above 60% are considered as close approximations for the sheet-like structures. Our numerical experiments show that this technique is more effective than the direct resolution reduction with regard to both shape similarity and element quantity. Moreover, the generated surface mesh can be utilized as constraints to generate corresponding volume mesh. The element quality of the volume mesh is high concerning a variety of measurements and the element quantity is reasonable for future finite element simulations. In general, the generated mesh models are competitive with grid models and have wide applications in both visualization and finite element simulation.

Acknowledgements

Support is gratefully acknowledged by ARC DP110103024. The authors are grateful to Ms. P. Liu from Research Institute of Petroleum Exploration & Development, China for providing the providing the micro-CT datasets used in this paper, and to the anonymous reviewers for the advice/comments that allowed this paper to be improved.

References

[1] S. Chen, Z.Q. Yue, L.G. Tham, Digital image-based numerical modeling method for prediction of inhomogeneous rock failure, Int. J. Rock Mech. Min. Sci. 41 (2004) 939–957.
[2] J. Gao, H. Xing, Z. Tian, H. Muhlhaus, Lattice Boltzmann modeling and evaluation of fluid flow in heterogeneous porous media involving multiple matrix constituents, Comput. Geosci. 62 (2014) 198–207.
[3] H.L. Xing, A. Makinouchi, P. Mora, Finite element modeling of interacting fault systems, Phys. Earth Planet. Inter. 163 (2007) 106–121.
[4] H.L. Xing, P. Mora, Construction of an intraplate fault system model of South Australia, and simulation tool for the iSERVO institute seed project, Pure Appl. Geophys. 163 (2006) 2297–2316.
[5] Y. Zhang, T.J.R. Hughes, C.L. Bajaj, An automatic 3D mesh generation method for domains with multiple materials, Comput. Methods Appl. Mech. Eng. 199 (2010) 405–415.
[6] D. Wildenschild, A.P. Sheppard, X-ray imaging and analysis techniques for quantifying pore-scale structure and processes in subsurface porous medium systems, Adv. Water Resour. 51 (2013) 217–246.

[7] V. Cnudde, B. Masschaele, M. Dierick, J. Vlassenbroeck, L.V. Hoorebeke, P. Jacobs, Recent progress in X-ray CT as a geosciences tool, Appl. Geochem. 21 (2006) 826–832.
[8] P. Iassonov, T. Gebrenegus, M. Tuller, Segmentation of X-ray computed tomography images of porous materials: a crucial step for characterization and quantitative analysis of pore structures, Water Resour. Res. 45 (2009).
[9] R.A. Ketcham, D.T. Slottke, J.M. Sharp, Three-dimensional measurement of fractures in heterogeneous materials using high-resolution X-ray computed tomography, Geosphere 6 (2010) 499–514.
[10] R. Quey, P.R. Dawson, F. Barbe, Large-scale 3D random polycrystals for the finite element method: Generation, meshing and remeshing, Comput. Methods Appl. Mech. Eng. 200 (2011) 1729–1745.
[11] H.L. Xing, W. Yu, J. Zhang, 3D mesh generation in geocomputing, in: Advances in Geocomputing, Springer-Verlag GmbH, 2009, pp. 27–64.
[12] B. Van Rietbergen, H. Weinans, R. Huiskes, B.J.W. Polman, Computational strategies for iterative solutions of large fem applications employing voxel data, Int. J. Numer. Methods Eng. 39 (1996) 2743–2767.
[13] F. Remondino, S. El-Hakim, Image-based 3D modelling: a review, The Photogrammetric Record 21 (2006) 269–291.
[14] K. Terada, T. Miura, N. Kikuchi, Digital image-based modeling applied to the homogenization analysis of composite materials, Comput. Mech. 20 (1997) 331–346.
[15] Z. Wu, J.M. Sullivan Jr, Multiple material marching cubes algorithm, Int. J. Numer. Methods Eng. 58 (2003) 189–207.
[16] D. Boltcheva, M. Yvinec, J.-D. Boissonnat, Mesh generation from 3D multi-material Images, in: Medical Image Computing and Computer-Assisted Intervention – MICCAI 2009, Springer, Berlin Heidelberg, 2009, pp. 283–290.
[17] T. Dey, F. Janoos, J. Levine, Meshing interfaces of multi-label data with Delaunay refinement, Eng. Comput. 28 (2012) 71–82.
[18] Y. Liu, H.L. Xing, Surface mesh generation of large-scale digital rock images in 3D, Proc. Comput. Sci. 18 (2013) 1208–1216.
[19] R.E. Guldberg, S.J. Hollister, G.T. Charras, The accuracy of digital image-based finite element models, J. Biomech. Eng. 120 (1998) 289–295.
[20] W.E. Lorensen, H.E. Cline, Marching cubes: a high resolution 3D surface construction algorithm, SIGGRAPH Comput. Graphics 21 (1987) 163–169.
[21] D.C. Banks, S.A. Linton, Counting cases in marching cubes: toward a generic algorithm for producing substitopes, IEEE Visual. (2003) 51–58.
[22] M. Bertram, G. Reis, R.H. van Lengen, S. Köhn, H. Hagen, Non-manifold mesh extraction from time-varying segmented volumes used for modeling a human heart, in: Proceedings of the Seventh Joint Eurographics/IEEE VGTC Conference on Visualization, 2005, pp. 199–206.
[23] Y. Zhang, C. Bajaj, Adaptive and quality quadrilateral/hexahedral meshing from volumetric data, Comput. Methods Appl. Mech. Eng. 195 (2006) 942–960.
[24] Y. Zhang, C. Bajaj, G. Xu, Surface smoothing and quality improvement of quadrilateral/hexahedral meshes with geometric flow, in: Proceedings of the 14th International Meshing Roundtable, Springer, 2005, pp. 449–468.
[25] M. Garland, P.S. Heckbert, Surface simplification using quadric error metrics, in: Proceedings of the 24th annual Conference on Computer Graphics and Interactive Techniques, 1997, pp. 209–216.
[26] H. Hoppe, Progressive meshes, in: Proceedings of the 23rd Annual Conference on Computer Graphics and Interactive Techniques, ACM, 1996, pp. 99–108.
[27] S. Valette, J.M. Chassery, R. Prost, Generic remeshing of 3D triangular meshes with metric-dependent discrete Voronoi diagrams, IEEE Trans. Visual. Comput. Graphics 14 (2008) 369–381.
[28] S. Valette, J.-M. Chassery, Approximated centroidal Voronoi diagrams for uniform polygonal mesh coarsening, Comput. Graphics Forum 23 (2004) 381–389.
[29] P. Alliez, E.C. de Verdire, O. Devillers, M. Isenburg, Isotropic surface remeshing, in: Proceedings of Shape Modeling International 2003, 2003, pp. 49–58.
[30] V. Surazhsky, P. Alliez, C. Gotsman, Isotropic remeshing of surfaces: a local parameterization approach, in: Proceedings of the 12th International Meshing Roundtable, 2003, pp. 215–224.
[31] P. Alliez, G. Ucelli, C. Gotsman, M. Attene, Recent advances in remeshing of surfaces, Shape Analysis and Structuring, Springer, Berlin Heidelberg, 2008, pp. 53–82.
[32] V. Kraevoy, A. Sheffer, Cross-parameterization and compatible remeshing of 3D models, ACM Trans. Graphics 23 (2004) 861–869.
[33] Q. Du, V. Faber, M. Gunzburger, Centroidal Voronoi tessellations: applications and algorithms, SIAM Rev. 41 (1999) 637–676.
[34] R.M. Haralick, S.R. Sternberg, X. Zhuang, Image analysis using mathematical morphology, IEEE Trans. Pattern Anal. Mach. Intell. PAMI-9 (1987) 532–550.
[35] S.H. Lo, Optimization of tetrahedral meshes based on element shape measures, Comput. Struct. 63 (1997) 951–961.
[36] J.R. Shewchuk, What is a good linear element? Interpolation, conditioning, and quality measures, in: Proceedings of the 11th International Meshing Roundtable, 2002, pp. 115–126.